PAPER • OPEN ACCESS

Velocity-space tomography of MeV-range fast-ion distributions in JET using wave–particle interaction priors

To cite this article: M. Rud *et al* 2025 *Nucl. Fusion* **65** 112006

OPEN ACCESS
IOP Publishing | International Atomic Energy Agency
Nuclear Fusion
Nucl. Fusion **65** (2025) 112006 (12pp)
https://doi.org/10.1088/1741-4326/ae1305

Velocity-space tomography of MeV-range fast-ion distributions in JET using wave–particle interaction priors

M. Rud[1,*], Y. Dong[2], L.-G. Eriksson[3], J. Eriksson[4], P.C. Hansen[2], O. Hyvärinen[5], H. Järleblad[2], Ye.O. Kazakov[6], D. Moseev[7], M. Nocente[8], B.C.G. Reman[6], A. Snicker[9], A. Valentini[1], M. Salewski[1] and JET Contributors[a]

[1] Department of Physics, Technical University of Denmark, 2800 Kgs. Lyngby, Denmark
[2] Department of Applied Mathematics and Computer Science, Technical University of Denmark, 2800 Kgs. Lyngby, Denmark
[3] Department of Space, Earth and Environment, Chalmers University of Technology, Gothenburg SE-412 96, Sweden
[4] Department of Physics and Astronomy, Uppsala University, 751 20 Uppsala, Sweden
[5] Department of Mathematics and Statistics, University of Helsinki, Helsinki FI-00014, Finland
[6] Laboratory for Plasma Physics, LPP-ERM/KMS, 1000 Brussels, Belgium
[7] Max-Planck-Institut für Plasmaphysik, Wendelsteinstr. 1, Greifswald 17491, Germany
[8] Department of Physics, University of Milano-Bicocca, 20126 Milano, Italy
[9] VTT, Technical Research Centre of Finland, Espoo, Finland

E-mail: mads.larsen@epfl.ch

Received 2 May 2025, revised 2 September 2025
Accepted for publication 14 October 2025
Published 27 October 2025

Abstract

The fast-ion distribution function in fusion plasmas can only be measured indirectly by solving an ill-posed inverse problem. The inversion being ill-posed necessitates regularisation of the problem to ensure that the reconstruction of the fast-ion distribution function depends smoothly on the measurements obtained by fast-ion diagnostics. In turn, the resulting reconstruction depends on the choice of regularisation, and it is therefore beneficial to choose a physics-informed prior as regularisation scheme. In this work, we reconstruct the high-energy tail in the MeV-range of the fast-deuterium distribution in JET discharges heated by waves in the ion cyclotron range of frequencies (ICRF) using neutron and gamma-ray emission spectroscopy. We do this by applying a physics-informed prior based on collision physics and a newly formulated ICRF-physics prior, and we compare these results with numerical simulations and inversions based on a standard Tikhonov regularisation scheme. Our findings suggest that the physics-informed regularisation scheme including the ICRF prior improves the reconstructions compared with standard Tikhonov regularisation. Finally, it is shown that constraining the reconstruction to have negative gradients in the directions of phase space dictated by ICRF physics results in a reconstruction that well resembles expectations based on ICRF physics theory and numerical simulations.

[a] See Maggi *et al* 2024 (https://doi.org/10.1088/1741-4326/ad3e16) for JET Contributors.
[*] Author to whom any correspondence should be addressed.

Keywords: fast ions, tomography, wave–particle interactions, JET

(Some figures may appear in colour only in the online journal)

1. Introduction

In the burning plasma regime of magnetic confinement fusion, the ions must be heated to temperatures of several keVs by energetic fusion alpha particles, which must be well confined from their birth in the MeV-range down to thermal energies. Electromagnetic wave heating in the ion cyclotron range of frequencies (ICRFs) is able to generate MeV ions, dubbed fast ions. It is of paramount importance to measure and understand the distribution function of fast ions, as they can drive instabilities in the plasma [1–7] and interact with instabilities and magnetohydrodynamic modes causing fast-ion transport from the core towards the edge [8–13]. The fast-ion velocity distribution function can be measured by velocity-space tomography [14–16] which has been used at ASDEX Upgrade [16–21], JET [22–24], MAST [25, 26], DIII-D [27], EAST [28–30], and is being studied for TCV [31], KSTAR [32] and ITER [33]. In this paper, we revisit two discharges of the Joint European Torus (JET) tokamak heated by ICRF heating generating fast deuterium ions in the MeV range. We reconstruct the fast-ion velocity distribution functions in the core of the plasma in discharges #86459 and #95679 by solving an ill-posed inverse problem using measurements of neutron emission spectroscopy (NES) and gamma-ray spectroscopy (GRS), as was done in [22] and [23], respectively. In discharge #86459, third-harmonic heating of deuterium is employed, with a cold resonance in the center of the plasma [34]. This generates a fast-ion tail up to MeV-range energies at approximately zero pitch in the center of the plasma. In discharge #95679, the three-ion heating scheme [35–38] is employed, with a cold resonance on the high-field side of the plasma. This generates a fast-ion tail of deuterium ions up to MeV-range energies with a non-zero pitch in the center of the plasma. The reconstruction of the high-energy tail in [22] used a smoothing regulariser, and the reconstruction in [23] used collision-physics regularisation as well as sparsity-promoting regularisation. However, it has recently been shown that wave–particle interactions between fast ions and the ICRF heating waves [39–41] can be incorporated as prior information in the inverse problem [42]. Here, we demonstrate that this new ICRF regularisation improves the reconstructions from experiments, in agreement with theory. Including the ICRF prior both confirms the conclusions of [22, 23], and results in reconstructions with fewer artefacts in agreement with theory.

We study the two JET discharges, #86459 and #95679, as they utilised qualitatively different ICRF heating scenarios, to study the flexibility of the ICRF regularisation and its ability to aid in the reconstruction of the fast-ion distribution in both cases. The theory behind these qualitative differences is briefly reviewed in section 3, and this is taken into account in the ICRF prior.

The paper is organised as follows: section 2 summarises the fast-ion diagnostic setup, which collected the data used in this study, in JET discharges #86459 and #95679. In section 3 we review the theory of the wave–particle interaction in the ICRFs needed to derive the streamlines in velocity space, along which we expect a fast-ion phase-space flow. The inverse problem of reconstructing the fast-ion distribution functions in discharges #86459 and #95679 is solved in section 4. Section 5 concludes the paper and provides an outlook.

2. Experimental setup

ICRF heated ions have been detected by FIDA [18, 43], NES [44–47], GRS [37, 38, 47–51], ion-cyclotron emission (ICE) [52], and NPA [53]. Our reconstructions are based on experimental data acquired by NES [44] and GRS [54]. Both discharges used the following neutron and gamma-ray generating reactions,

$$ {}^2_1\mathrm{D} + {}^2_1\mathrm{D} \longrightarrow {}^3_2\mathrm{He} + \mathrm{n}\,(2.45\mathrm{MeV})\,, \tag{1} $$

$$ {}^2_1\mathrm{D} + {}^9_4\mathrm{Be} \longrightarrow {}^{10}_5\mathrm{B}^* + \mathrm{n}, $$

$$ {}^{10}_5\mathrm{B}^* \longrightarrow {}^{10}_5\mathrm{B} + \gamma\,(2.868\mathrm{MeV})\,, \tag{2} $$

$$ {}^2_1\mathrm{D} + {}^9_4\mathrm{Be} \longrightarrow {}^{10}_4\mathrm{Be}^* + {}^1_1\mathrm{H}, $$

$$ {}^{10}_4\mathrm{Be}^* \longrightarrow {}^{10}_4\mathrm{Be} + \gamma\,(3.367\mathrm{MeV})\,. \tag{3} $$

The NES diagnostics utilise the reaction in (1), and the GRS diagnostics utilise the reactions in (2) and (3).

The diagnostic sensitivity to each part of velocity space is quantified in so-called weight functions. The weight function w is defined as the kernel function that maps the fast-ion distribution function f to the diagnostic signal s according to [55–60]

$$ s\,(E_{\mathrm{d}1}, E_{\mathrm{d}2}, \varphi) = \int w\,(E_{\mathrm{d}1}, E_{\mathrm{d}2}, \varphi, \mathbf{x}, \mathbf{v}) f(\mathbf{x}, \mathbf{v})\, \mathrm{d}\mathbf{x}\, \mathrm{d}\mathbf{v}, \tag{4} $$

where $E_{\mathrm{d}1}$ and $E_{\mathrm{d}2}$ denote the measurement bin edges of the diagnostic with finite resolution, φ is the viewing angle between the line of sight and the magnetic field in the (R, z) point of interest in position space, and $\mathbf{x}$ and $\mathbf{v}$ are the Cartesian position-space and velocity-space coordinates. The weight functions have units of signal/ion, and the integrations are effectively evaluated in a small finite region around the (R, z) point of interest. In this study we reconstruct the fast-ion distribution function in velocity space for a small region around the plasma core, where most neutrons and gamma-rays are generated [22, 23]. In addition to this, for NES the reconstruction rests on the appropriate assumption that the neutrons mainly originate from beam-target reactions, where fast ions

react with thermal ions compared to thermal-thermal or beam-beam reactions [22, 23]. This assumption is always very well fulfilled for two-step reaction GRS. Velocity-space weight functions have been calculated for several different fast-ion diagnostics, such as FIDA spectroscopy [55, 61–63], collective Thomson scattering (CTS) [33, 64–66], GRS [67, 68], NES [22, 69, 70], fast-ion loss detectors [71, 72], ICE [73, 74] and 3 MeV proton diagnostics [75]. Weight functions have also been calculated in 3D phase space for one-step NES and GRS diagnostics [57, 58], for two-step GRS diagnostics [76], for neutron diagnostics, neutral particle analysers and FIDA spectroscopy [56], as well as for a general-type diagnostic based on projected velocities [77].

The weight functions are calculated using the orbit-weight computational framework (OWCF) code [59] interfaced with the DRESS code [78] for NES and with GENESIS for GRS [50, 79]. Discretising the integral equation (4) allows us to express the relation as a matrix-vector product,

$$\mathbf{s} = W\mathbf{f}, \tag{5}$$

where each row in the matrix W is a weight function, $\mathbf{s}$ is the diagnostic signal collected in a column vector, and $\mathbf{f}$ is the vectorised fast-ion distribution function.

2.1. Third-harmonic ICRF-heating scenario

In discharge #86459 the plasma was heated by 4.5 MW of neutral beam injection (NBI) with beam injection energies of 80 keV, 100 keV and 120 keV (and their corresponding half and one-third energies), and 3 MW of third harmonic ICRF heating. The ICRF wave frequency was 51 MHz and the magnetic field on axis was $B_0 = 2.25$ T. The electron density was approximately 4×10^{19} m^{-3}. The experimental data used in this work is the average of the data collected in the time period from 50.5 s to 52.1 s in the discharge. Three NES detectors and one high-purity Germanium (HpGe) [51] were used. One neutron detector, time of flight optimised for high rates (TOFORs) [80, 81], measures the time of flight of neutrons traversing the diagnostic instrument and has a line of sight that is almost perpendicular to the magnetic field. The two oblique NES detectors, the single-crystal diamond detector and the liquid scintillator NE213 [82], share a line of sight, which has an angle of 47° with respect to the magnetic field on axis, which is therefore vital when aiming to resolve the fast-ion distribution function in pitch. The neutrons mainly originate from the DD reaction in equation (1), to which the TOFOR diagnostic is optimised [80, 81]. The spectrum formation for beam-target reactions gives direct access to the velocity of the energetic particles [83, 84]. The HpGe GRS detector, measuring a spectrum of gamma-ray energies, shares the perpendicular line of sight with TOFOR. The spectral broadening, caused by the Doppler shift due to the motion of the fast deuterium population, around the 2.868 MeV and 3.367 MeV peaks of nominal energy, is used for the inference of the fast-ion distribution function [85]. These spectral lines originate from the two two-step nuclear reactions in equations (2) and (3) [51].

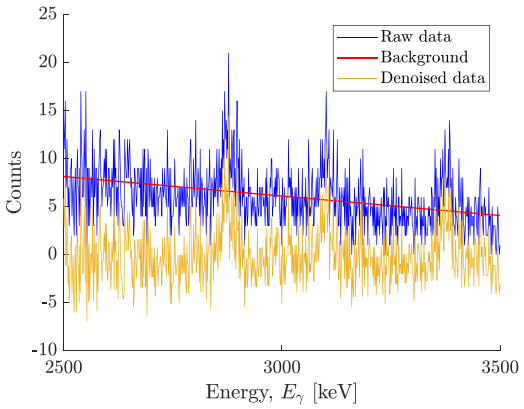

Figure 1. Subset of the HpGe data in discharge #86459. The raw data is shown in blue, and the data following background subtraction is shown in yellow. The background estimation is given by the red line.

The processing of the experimental data of this discharge follows that of [22], but is described in the following for completeness. Since we are only interested in reconstructing the high-energy tail of the fast-ion distribution function above the neutral beam injection energy, the measurement data points also sensitive to contributions from velocity space below 120 keV are discarded. This is because the fast-ion densities in the high-energy tail are significantly smaller than the densities around the NBI energy. The retained and discarded measurements are visualised in figures 2 and 4 in [22]. We keep only measurement data points corresponding to weight functions with a non-zero sensitivity somewhere in our target velocity space. In addition to this, we de-trend the gamma-ray data according to a linear polynomial as shown in figure 1. The weight functions are rescaled with a single factor per spectrum, such that the synthetic data calculated from the matrix-vector product of the weight matrix and the ASCOT-RFOF [51, 86] simulation of the discharge $W\mathbf{f}_{\mathrm{ASCOT}}$ matches the amplitude of the experimental data. This is also shown in figures 2 and 4 in [22]. To treat all diagnostics on an equal footing, the weight functions and the experimental data are weighted with the maximum value of the obtained measurements for each diagnostic individually. Following this post-processing we end up with a set of measurements collected in the single vector $\mathbf{s}$ (see equation (5)), which is shown in figure 2. This is the data used for the reconstruction of the fast-ion distribution function in discharge #86459.

2.2. Three-ion scheme ICRF-heating scenario

For discharge #95679, the data used in the present work to infer the high-energy tail of the fast-ion distribution function is an average of the data collected between time $t = 8$ s and $t = 9$ s in the discharge. The data is composed of four spectra in total collected by three diagnostic instruments, as the single-crystal diamond detector was not available for this shot. Thus, the spectra are collected by the TOFOR diagnostic, an oblique NE213 diagnostic [87], and the HpGe GRS diagnostic.

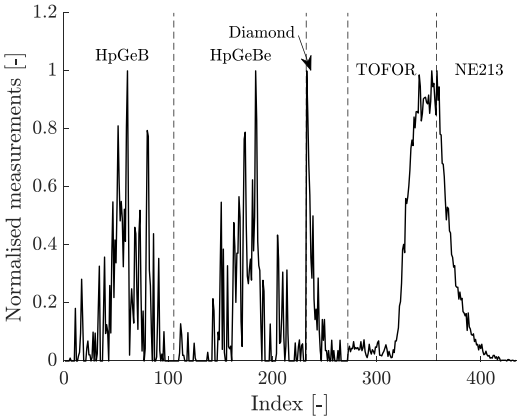

Figure 2. Rescaled and normalised data used for the reconstruction of the fast-ion distribution function in discharge #86459. Total number of data points: 434.

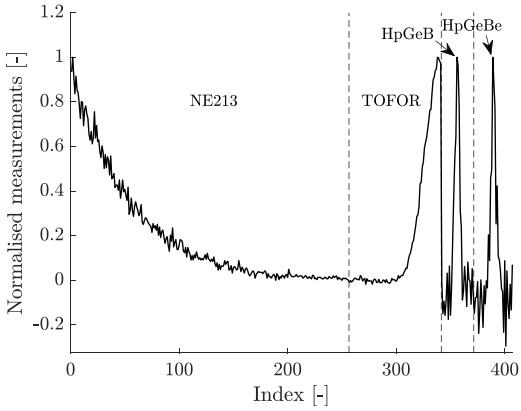

Figure 3. Rescaled and normalised data used for the reconstruction of the fast-ion distribution function in discharge #95679. Total number of data points: 407.

As per the procedure in [23], the weight matrix W for each diagnostic calculated by the OWCF is rescaled using the TRANSP distribution [88] of the corresponding discharge. The weight matrix of a specific diagnostic is rescaled, such that the maximum of the synthetic measurements calculated from (5) matches the maximum of the experimental data collected by the same diagnostic. This is done for all four diagnostics and is also shown in figure 8 in [23].

We note that the ASCOT-RFOF simulation result and the TRANSP simulation result are used for the two discharges respectively as those were chosen for the analysis in [22, 23]. In this work, the simulation results are not to be considered the ground truths. They serve to compare experimental measurements with modelling, and it is considered beyond the scope of this work to benchmark the codes against each other.

Since we are not attempting to reconstruct the distribution function below the NBI energy, we discard all weight functions polluted by the NBI, and the corresponding measurements, as we did in the previous case. This is visualised in figure 8 in [23]. Again, we keep only those weight functions that have a non-zero sensitivity somewhere in our target velocity space, i.e. any zero rows in W are removed from the problem. In order to treat all diagnostics on the same footing in the inverse problem, we weight the measurements and the weight functions with the maximum value of the obtained measurements for each diagnostic individually as for discharge #86459. Following this post-processing of the data we end up with a set of measurements collected in the single vector $\mathbf{s}$ (5) used for the inversion. The post-processed data is shown in figure 3.

3. Characteristics of ion motion in velocity space for ICRF heating

The ICRF heating wave can exchange energy with ions in the plasma if the following resonance condition is satisfied [40],

$$\omega = n\omega_{ci} + k_{\parallel} v_{\parallel}, \tag{6}$$

where ω is the angular frequency of the heating wave, $\omega_{ci} = qB(R,z)/m$ is the local cyclotron frequency, q is the electric charge of the particle, m is the particle mass, n is an integer harmonic, $k_{\parallel}$ is the parallel component of the wave vector of the heating wave, and $v_{\parallel}$ is the component of the ion velocity parallel to the magnetic field. The velocity-space characteristics of the wave–particle interaction can be derived from the corresponding changes in energy E, toroidal canonical angular momentum P_{ϕ} and normalised magnetic moment Λ, which are invariants of the motion in the absence of electric fields. From these, we can deduce the change in the velocity component perpendicular to the magnetic field $v_{\perp}$ given a change in $v_{\parallel}$,

$$\Delta v_{\perp} = \frac{1 - p_{\infty}^2}{p_{\infty}^2} \frac{v_{\parallel}}{v_{\perp}} \Delta v_{\parallel}, \tag{7}$$

where p_{∞} is the asymptotic pitch value for large energy gains. The vectors tangent to the streamlines in velocity space are thus given by

$$\boldsymbol{\epsilon} = \begin{pmatrix} \Delta v_{\parallel} \\ \Delta v_{\perp} \end{pmatrix} = \begin{pmatrix} 1 \\ \frac{1-p_{\infty}^2}{p_{\infty}^2} \frac{v_{\parallel}}{v_{\perp}} \end{pmatrix} \Delta v_{\parallel}. \tag{8}$$

The asymptotic streamline for large energy gains is given by

$$v_{\perp,\infty}^2 = \frac{\Lambda_{\infty}}{B_0/B(R,z) - \Lambda_{\infty}} v_{\parallel,\infty}^2, \tag{9}$$

where B_0 is the magnetic field on axis and $B(R,z)$ is the local magnetic field. For more details on the Λ_{∞} parameter, we refer the reader to appendix A. Here, we just note that if the cyclotron cold resonance line of the ICRF wave is located on the magnetic axis, then $\Lambda_{\infty} = 1$, whereas $\Lambda_{\infty} \neq 1$ if the cyclotron resonance line is located off axis. The streamlines in the core of the plasma for discharges #86459 and #95679 are shown in figure 4. In both cases, the streamlines in velocity space are drawn in the (R,z) coordinate pair of the magnetic axis. Contrary to 3D streamlines as in [42], a single ion does not move along the streamlines in velocity space as shown in figure 4. The ion moves to a different (R,z) location

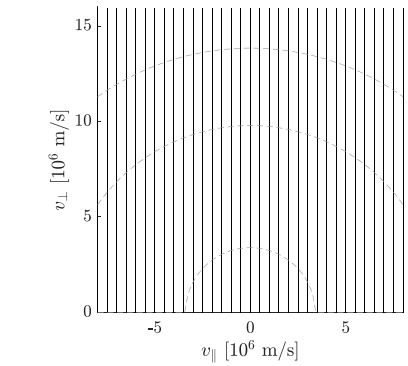

(a) Third-harmonic on-axis resonance #86459

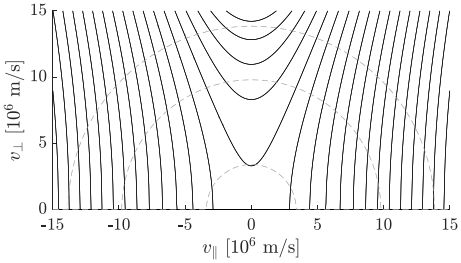

(b) Three-ion scheme with off-axis resonance #95679

Figure 4. ICRF streamlines in velocity space on the magnetic axis for the JET discharges (*a*) #86459 and (*b*) #95679. The gray dashed semicircles denote the energy contours of 120 keV, 1 MeV and 2 MeV, respectively.

and is therefore not observed further. Instead, the velocity-space streamlines can be understood as a 'wind' of ions one would encounter if one was standing in a single (R, z) location. The streamlines in velocity space look different depending on where in (R, z)-space they are drawn, and where the resonance line is located. In discharge #86459, third-harmonic ICRF heating was used, where the resonance line traverses the magnetic axis, such that $\Lambda_\infty = 1$. The streamlines therefore point in the $v_\perp$ direction. Contrary to this, in discharge #95679 the three-ion scheme was used, where the wave absorption happens in the core, but $\Lambda_\infty < 1$, such that the resonance line traverses the high-field side. This results in the tilted streamlines when observing the ions around the axis. The tilt of the streamlines is a consequence of conservation of magnetic moment [37, 42], which also leads to the so-called rabbit ear distribution [89, 90]. To satisfy the resonance condition in the core, the fast ions must therefore provide a Doppler shift, resulting in primarily fast-ions with $v_\parallel > 0$ absorbing wave energy. The theory thus predicts that the high-energy tail of the fast-ion distribution function is drawn in the $v_\perp$-direction in discharge #86459, whereas it is drawn with a tilt towards positive pitches in discharge #95679.

4. The inverse problem and regularisation

To infer the fast-ion distribution function $\mathbf{f}$ given $\mathbf{s}$ and W it is not feasible to do a standard least squares minimisation, due to the ill-posedness of the inverse problem [91]. As the weight matrix is ill-conditioned, noise in the data will be amplified in the inversion, rendering the result useless. To circumvent this issue, we regularise the problem by adding an additional term in the least squares minimisation, with Tikhonov regularisation being a popular choice. The general Tikhonov solution [92] is given by

$$\bar{\boldsymbol{f}}_\lambda = \arg\min_{\mathbf{f}} \left(\|\mathbf{s} - W\mathbf{f}\|_2^2 + \lambda^2 \|L\mathbf{f}\|_2^2 \right), \tag{10}$$

where L is a regularisation matrix chosen to penalise a specific property of the solution. Prior information can be incorporated by an appropriate choice of regularisation matrix. The regularisation parameter λ controls the strength of the regularisation relative to the data fidelity term. Choosing the optimal regularisation parameter is not trivial, and an overview of different choosing methods can be found in chapter 5 of [93]. As one method cannot be favored over others, in this work we combine visual inspection with comparison to the ASCOT-RFOF simulation of discharge #86459 and the TRANSP simulation of discharge #95679.

A popular choice of regularisation matrix is to use the finite-difference approximation of the gradient operator, denoted by L_1, which promotes smooth solutions. The motivation for this choice is that Coulomb collision between particles in the plasma tends to render the distribution function smooth. The same is the case for the diffusive nature of the wave–particle interactions in ICRF heating. In this paper, we compare the performance of this choice of regularisation matrix to regularisation matrices based on physics-informed prior information of collision physics and ICRF physics, which includes knowledge of the actual physics acting to smoothen the distribution function, contrary to the previous choice of regularisation.

The collision physics regularisation [24, 28, 94] was also employed in [23] to reconstruct the fast-ion distribution function in discharge #95679, where the fast-ion distribution function is expanded in a set of slowing-down distribution functions [95, 96]. However, in this study we employ different expansion functions. Instead of using full slowing-down distribution functions as expansion functions, we dampen the slowing-down distribution functions around the source injection points, as in [28], since we only need the correlation between each point in velocity space and the points in its near vicinity. This avoids the significant assumption of collisional regularisation based on slowing-down functions generated by following fast ions all the way from injection until thermalisation. This type of collision regularisation implicitly assumes correlations between pixels far apart in phase space, which we avoid. The dampened expansion functions in (v, p) space are given by

$$\hat{f}_{\mathrm{sd}}(v,p) = f_{\mathrm{sd}}(v,p)\,\mathrm{erfc}\left(\frac{v - v_0}{\sigma_v}\right)\mathrm{erfc}\left(\frac{v_0 - v}{5\sigma_v}\right), \tag{11}$$

where $\mathrm{erfc}(z)$ is the complementary error function, and we have chosen $\sigma_v = 0.5 \cdot 10^6\,\mathrm{m\,s^{-1}}$. The slowing-down distribution functions in [95, 96] are derived for a homogeneous plasma, which is not the case in a tokamak. The longer a particle stays in the plasma, the larger the distance of that

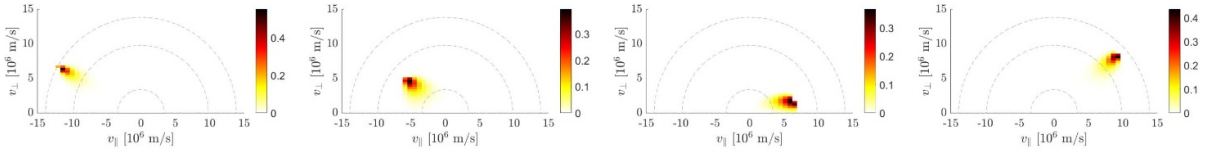

Figure 5. Subset of normalised expansion functions, given by equation (11), collectively defining the collision physics regularisation. The curved semicircles are the 120 keV, 1 MeV and 2 MeV isocurves, respectively.

particle from the source point in velocity space becomes due to the slowing-down process. Additionally, the longer the particle stays in the plasma, the larger the effect of the plasma inhomogeneity and any anomalous transport processes will be. Therefore, the larger the distance in velocity space, the less accurate the prior information of a particle slowing down in a homogeneous plasma becomes for a particle slowing down in a tokamak plasma with possible anomalous transport. Therefore, σ_v is chosen to be so small that only nearby pixels in velocity space are correlated via the slowing-down distributions. The slowing-down distributions f_{sd} are given by [95, 96]

$$f_{\mathrm{sd}}(v,p) = \frac{1}{2\sqrt{\pi\alpha}} \frac{S\tau_s}{v^3 + v_c^3} \mathrm{e}^{-\frac{(p-p_0)^2}{4\alpha}}, \tag{12}$$

where the source strength S and the Spitzer slowing-down time τ_s can be absorbed in a normalisation, v_c is the critical velocity at which ion-ion collisions are equally as strong as ion-electron collisions, and

$$\alpha = \frac{\pm\beta\left(1-p_0^2\right)}{3} \log\left(\frac{1+\left(v_c/v\right)^3}{1+\left(v_c/v_0\right)^3}\right), \tag{13}$$

where $\beta = m_{\mathrm{ti}} Z_1 / 2m_{\mathrm{fi}} = 1/2$ with m_{ti} and m_{fi} being the masses of the thermal and fast ions, respectively, and Z_1 is the effective ion charge. The $+\beta$ solution is used for $v < v_0$ and the $-\beta$ solution is used for $v \geqslant v_0$. Examples of expansion functions for the discharge #95679 are shown in figure 5. Note that the expansion functions at higher speeds, which are in the electron collision dominated regime, are elongated in the radial direction, corresponding to little pitch angle scattering, as in figures 5(*a*) and (*d*). On the contrary, the expansion functions at lower speeds, where ion collisions become more important, are broader, corresponding to more pitch angle scattering, as in figures 5(*b*) and (*c*). The expansion functions $\hat{f}_{\mathrm{sd}}$ are normalised to unity when employed as regularisation. Equivalent expansion functions for discharge #86459 are used for the reconstructions of the fast-ion distribution function in that discharge. The expansion of the fast-ion distribution function in slowing-down functions in the discrete case is given by

$$\mathbf{f} = \sum_{j=1}^{M} c_j \hat{f}_{\mathrm{sd},j} = X\mathbf{c}, \tag{14}$$

where an expansion-function source is placed in all pixels in velocity space, and where each column in the matrix X is an expansion function, and $\mathbf{c}$ is the vector of expansion coefficients. With a source point at all points in velocity space, X is square, and the task is no longer to reconstruct $\mathbf{f}$ in itself, but to reconstruct the coefficients $\mathbf{c}$. Penalising the two-norm of the coefficient vector $\mathbf{c}$ in the inverse problem has been shown to be equivalent to regularising $\mathbf{f}$ according to collision physics [28, 94]. In [23], the one-norm of $\mathbf{c}$ was penalised to promote sparsity.

As mentioned, in addition to the collision physics regularisation we also regularise according to ICRF physics. As in [42], the ICRF regularisation is implemented as a modification to the finite-difference approximation of the gradient operator L_1, which ensures that only neighbouring pixels in phase space are assumed correlated with this ICRF physics regularisation. In addition to this, the ICRF regularisation penalises those solutions of the inverse problem that are not consistent with the wave–particle interaction theory, such that the reconstructions do not only rely on collision physics prior information. This is beneficial in situations with sparse datasets due to a limited number of available fast-ion diagnostics. However, there is a difference between the ICRF regularisation in this work and the ICRF regularisation in [42]. The ICRF regularisation in [42] was imposed in the 3D phase space of invariants (E, P_ϕ, Λ), where the streamlines represent actual trajectories that ions follow in phase space if interacting with the ICRF wave. Instead, in this work, the ICRF regularisation is imposed in 2D velocity space, as also discussed in section 3. Here, each individual particle receiving a kick in velocity space will be transferred to a slightly different drift orbit and thus move away from the (R, z) location we consider. Nevertheless, the streamlines represent a 'wind' of ions traversing a single (R, z) location. This 2D case can be considered a projection of the 3D case onto a single (R, z) point.

The ICRF regularisation in velocity space only depends on the heating-wave frequency and the magnetic field strength on axis and in the point of interest and can therefore easily be adapted from experiment to experiment, and across machines. In order to penalise the gradients along the ICRF streamlines, the gradient in each point in velocity space is projected onto the tangent vectors given in (8) by the projection matrix

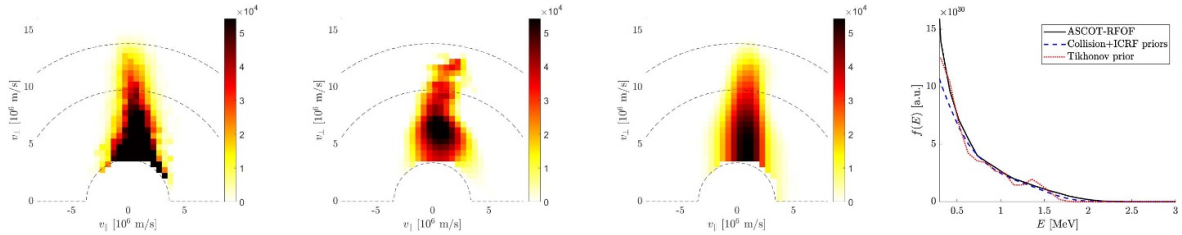

(a) ASCOT-RFOF (b) First-order Tikhonov prior (c) Collisions and ICRF prior (d) 1D distribution

Figure 6. (*a*) High-energy tail above the neutral beam injection energy from ASCOT-RFOF distribution of discharge #86459. (*b*) Reconstruction of the high-energy tail of the fast-ion distribution function using first-order Tikhonov regularisation. (*c*) Reconstruction of the high-energy tail of the fast-ion distribution function using both collision physics regularisation and ICRF regularisation. All colourbars are cut off at the maximum of (*c*). (*d*) 1D distributions $f(E)$ integrated over pitch.

$$\begin{aligned}\hat{\boldsymbol{\epsilon}}_m\hat{\boldsymbol{\epsilon}}_m^T &= \frac{1}{\|\boldsymbol{\epsilon}_m\|^2}\begin{pmatrix}\left(\Delta v_\parallel\right)^2 & \Delta v_\parallel \Delta v_{\perp,m}\\ \Delta v_{\perp,m}\Delta v_\parallel & \left(\Delta v_{\perp,m}\right)^2\end{pmatrix}\\ &= \frac{\left(\Delta v_\parallel\right)^2}{\|\boldsymbol{\epsilon}_m\|^2}\begin{pmatrix}1 & \frac{1-p_\infty^2}{p_\infty^2}\frac{v_{\parallel,m}}{v_{\perp,m}}\\ \frac{1-p_\infty^2}{p_\infty^2}\frac{v_{\parallel,m}}{v_{\perp,m}} & \left(\frac{1-p_\infty^2}{p_\infty^2}\frac{v_{\parallel,m}}{v_{\perp,m}}\right)^2\end{pmatrix},\end{aligned} \tag{15}$$

where $\boldsymbol{\epsilon}$, $\Delta v_\parallel$ and $\Delta v_\perp$ are given by (8), and $m = 1,\ldots,M$ is the velocity-space pixel index with M being the total number of pixels in velocity space. In units of $\left(\Delta v_\parallel\right)^2/\|\boldsymbol{\epsilon}_m\|^2$, the ICRF regularisation matrix $L_1^{(\mathrm{IC})}$ is then [97]

$$L_1^{(\mathrm{IC})} = \begin{pmatrix}\mathbf{I}_M & \mathbf{D}_{v_\parallel v_\perp}\left(\mathbf{v}_\parallel,\mathbf{v}_\perp\right)\\ \mathbf{D}_{v_\perp v_\parallel}\left(\mathbf{v}_\parallel,\mathbf{v}_\perp\right) & \mathbf{D}_{v_\perp v_\perp}\left(\mathbf{v}_\parallel,\mathbf{v}_\perp\right)\end{pmatrix} L_1, \tag{16}$$

where $\mathbf{I}_M$ is the $M\times M$ identity matrix, and $\mathbf{D}_{ij}$ are $M\times M$ diagonal matrices with the m'th element along the diagonal being the i,j'th element of (15). In addition to this, we also require that the fast-ion distribution function must be non-negative. The minimisation problem to solve is then

$$\begin{aligned}\bar{\boldsymbol{c}}_\lambda = \arg\min_{\mathbf{c}}&\left(\|\mathbf{s}-WX\mathbf{c}\|_2^2+\lambda^2\|\mathbf{c}\|_2^2+\lambda_{\mathrm{IC}}^2\|L_1^{(\mathrm{IC})}X\mathbf{c}\|_2^2\right)\\ &\text{subject to } X\mathbf{c}\geqslant\mathbf{0},\end{aligned} \tag{17}$$

such that

$$\bar{\boldsymbol{f}}_\lambda = X\bar{\boldsymbol{c}}_\lambda, \tag{18}$$

where λ and λ_{IC} are the regularisation parameters controlling the strength of the collision-physics regularisation and the ICRF-physics regularisation, respectively.

4.1. Reconstructions

In figure 6, we compare the ASCOT-RFOF distribution function in a small volume around the magnetic axis of discharge #86459 (figure 6(*a*)) with reconstructions using different regularisations. A reconstruction employing first-order Tikhonov regularisation is shown in figure 6(*b*) and a reconstruction employing collision physics and ICRF regularisation is shown in figure 6(*c*). Regularisation parameter scans of the reconstructions are shown in appendix B. The reconstructions in figures 6(*b*) and (*c*) are also shown in figures B1(*c*) and B2(*g*). One-dimensional distributions in energy are shown in figure 6(*d*), which are obtained by integration of the 2D functions over pitch [98]:

$$f(E) = \int_{-1}^{1} f\left(p\sqrt{\frac{m}{2E}}, \sqrt{\frac{2E}{m}\left(1-p^2\right)}\right)\left|\frac{\partial\left(v_\parallel,v_\perp\right)}{\partial\left(E,p\right)}\right|\mathrm{d}p, \tag{19}$$

where the Jacobian of the coordinate transformation is

$$\left|\frac{\partial\left(v_\parallel,v_\perp\right)}{\partial\left(E,p\right)}\right| = \frac{1}{m\sqrt{1-p^2}}. \tag{20}$$

It is evident that the high-energy tails of the reconstructions match that of the ASCOT-RFOF computation. The ASCOT-RFOF distribution increases strongly towards the NBI region. The tomographic reconstructions has no information about such low energies. All colourbars of figure 6 are thus cut off at the maximum of figure 6(*c*). The overall shape of the reconstruction using the ICRF prior has a better match with ASCOT-RFOF, as it is slimmer and smoother and does not have the slight bump-on-tail appearing in the reconstruction using only Tikhonov regularisation, which is most likely an artefact. Above a certain fast-ion energy, finite Larmor radius effects will reduce the wave–particle interaction strength. This region in energy is referred to as the barrier region, and it is expected to occur at around 2 MeV in this discharge [34] with third-harmonic heating, such that the tail is not dragged to higher energies. Without enforcing it in the inversion, our reconstructions reflect this property predicted by theory.

In figure 7, we compare the TRANSP distribution function in a small volume around the magnetic axis of discharge #95679 with reconstructions employing first-order Tikhonov regularisation and collision physics and ICRF regularisation. In figure 7(*d*) we compare the 1D distributions in energy.

As in the on-axis resonance case, the trend of the high-energy tails of the reconstructions follow that of the numerical computation well, this time calculated by TRANSP. All colourbars in figure 7 are thus cut off at the maximum of figure 7(*c*). Regularisation parameter scans of the reconstructions are shown in appendix B. The reconstructions in figures 7(*b*) and (*c*) are also shown in figures B3(*c*) and B4(*g*). We notice that the depleted region of phase-space density in $v_\parallel$ as predicted by the TRANSP simulation is not measured by

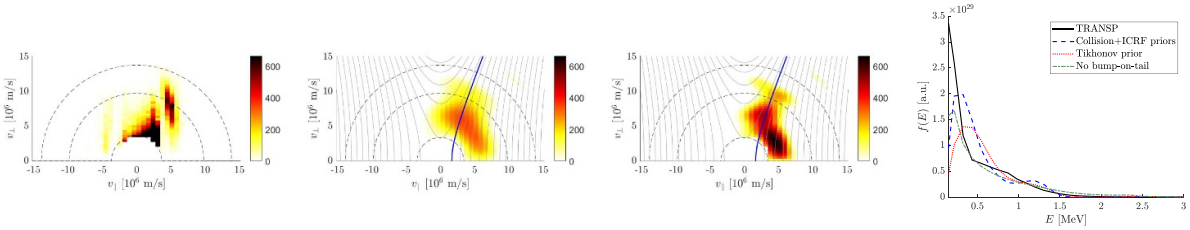

(a) TRANSP distribution (b) First-order Tikhonov prior (c) Collisions and ICRF prior (d) 1D distributions

Figure 7. (*a*) High-energy tail above the neutral beam injection energy from TRANSP distribution of discharge #95679. (*b*) Reconstruction of the high-energy tail of the fast-ion distribution function using first-order Tikhonov regularisation. (*c*) Reconstruction of the high-energy tail of the fast-ion distribution function using both collision physics regularisation and ICRF regularisation. All colourbars are cut off at the maximum of (*c*). (*d*) 1D distributions $f(E)$ integrated over pitch. The blue line denote the ICRF characteristic expected from initial energy of 110 keV and pitch $v_\parallel/v = 0.6$.

the tomography. The combination of the collision-physics regularisation and ICRF regularisation enables a reconstruction with a narrow tail in accordance with the expectations from the wave–particle interactions, while simultaneously obtaining a small bump on tail, which is not expected. On the contrary, the reconstruction with first-order Tikhonov regularisation appears to be broader in pitch than expected from the simulation as a result of the required smoothing. This leads to a smaller peak in the high-energy tail and a less pronounced orientation along the streamlines than expected from ICRF physics. Here, the combined use of collision-physics regularisation and ICRF regularisation outperforms first-order Tikhonov regularisation. On the other hand, the reconstructions show a region relatively broad in pitch near the NBI energy at $v_\parallel > 0$ compared with the TRANSP distribution. This is expected to be due to the higher diagnostic sensitivity to co-going ions than counter-going ions and due to the sparsity of the measurement data.

The use of regularisation is inevitable, but it is preferred to apply as little regularisation as possible, such that the reconstruction is determined primarily by the obtained measurements. However, as demonstrated in this work, strong physics-informed prior information is an advantage in situations with sparse datasets. To this end, we present a reconstruction using an additional piece of prior information. Because ICRF heating is a diffusive process in phase space, the effect of the wave absorption is loosely speaking to smooth out the distribution function along the energy direction. On its own, it can therefore not create a bump-on-tail feature in the energy direction for a given Λ (A.2) and P_ϕ (A.3), and therefore no bump-on-tail in the distribution function of fast deuterons is expected. On top of this, there is no evidence of a bump-on-tail present in the neutron spectra from this discharge in the time window of interest, as presented in figure 3. Examples of such spectra can be seen in [99]. To use this as prior information, we can add the constraint to the inverse problem that the gradient of the fast-ion distribution function along the ICRF streamlines must be negative towards higher energies. The minimisation problem to solve is then the same as in equation (17) with the additional constraint $L_1^{(\mathrm{IC})} X\mathbf{c} \leqslant \mathbf{0}$. A reconstruction with this additional constraint is shown in figure 8. Here we also show the streamlines to emphasise the direction of the tail distribution.

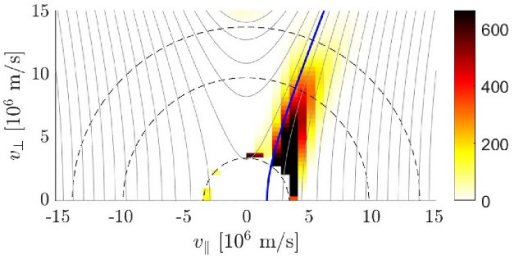

Figure 8. Reconstruction of the high-energy tail distribution of discharge #95679 including the monotonicity constraint along the streamlines. Colourbar and blue line as in figure 7.

The one-dimensional distribution in energy of this reconstruction is also visualised in figure 7(*d*) by the green dashed-dotted line.

5. Conclusion and outlook

The study has shown the reconstructions of the tails of ICRF-heated fast-ion distribution functions in velocity space using physics-informed prior information in the form of collision physics and ICRF physics. By comparing these reconstructions with reconstructions from previous studies using first-order Tikhonov regularisation and collision-physics regularisation without ICRF regularisation, it has furthermore been shown how the addition of physics-informed prior information results in less artefacts in the fast-ion distribution function, while at the same time limiting correlations between pixels far apart in phase space, as can be the case in collision physics regularisation. Specifically, the inclusion of the ICRF prior to reconstruct the fast-ion distribution function in discharge #86459 results in a smooth and narrow high-energy tail extending in the $v_\perp$ direction. For discharge #95679, regularising according to ICRF physics results in a definite high-energy tail tilted towards positive pitches in accordance with theory, and the combination of collision-physics and ICRF-physics priors results in a narrower tail compared with the Tikhonov regularisation counterpart. In addition to this, constraining the reconstruction to have negative gradients along the streamlines results in a reconstruction that well resembles

expectations based on ICRF physics theory and the TRANSP simulation result. Different regularisation techniques result in different reconstructions. However, all reconstructions share the main physical properties, such as the direction of the tilt of the high-energy tail in velocity space.

We expect that the physics-based prior information of collision physics and ICRF physics will be essential for the feasibility of reconstructions in phase space as recently demonstrated by orbit tomography [100]. The 2D formalism exploiting these physics-informed priors are in fact derived for phase-space tomography in 3D–5D [42, 77, 94, 97, 101]. Future work will attempt 3D–5D phase-space tomography using the prior information in the same way as we demonstrate here experimentally for 2D velocity-space tomography.

As an extension to the wave–particle interaction prior, a next step is to incorporate interactions between fast ions and Alfvén eigenmodes and neoclassical tearing modes, which are of lower frequency than the ICRF heating wave. In this case, the magnetic moment is conserved, altering the changes in the constants of motion from the ICRF heating case. In addition to this, the resonance condition is different, as it must take into account orbital frequencies given by poloidal and toroidal transit times of the fast-ion orbits.

Acknowledgment

This work was supported by the Villum Synergy Grant No. VIL50096 from the Villum Foundation.

This work has been carried out within the framework of the EUROfusion Consortium, funded by the European Union via the Euratom Research and Training Programme (Grant Agreement No. 101052200 - EUROfusion). Views and opinions expressed are however those of the author(s) only and do not necessarily reflect those of the European Union or the European Commission. Neither the European Union nor the European Commission can be held responsible for them.

Appendix A. Derivation of velocity-space characteristics

In the appendix, we derive the velocity-space characteristics of the wave–particle interaction from the corresponding changes in energy E, toroidal canonical angular momentum P_ϕ and normalised magnetic moment Λ, which are invariants of the motion in the absence of electric fields. The invariants of the motion are defined by

$$E = \frac{1}{2} m \left(v_\parallel^2 + v_\perp^2 \right), \tag{A.1}$$

$$\Lambda = \frac{\mu B_0}{E} = \frac{m v_\perp^2}{2B} \frac{B_0}{E}, \tag{A.2}$$

$$P_\phi = mR \frac{B_\phi}{B} v_\parallel + q \Psi_p, \tag{A.3}$$

where $v_\perp$ is the particle velocity component perpendicular to the magnetic field, μ is the magnetic moment, B_0 is the magnetic field on axis, $B = B(R,z)$ is the local magnetic field, $B_\phi = B_\phi(R,z)$ is the toroidal component of the magnetic field, R is the major radial coordinate, and $\Psi_\mathrm{p} = \Psi_\mathrm{p}(R,z)$ is the poloidal magnetic flux per radian. In the case of resonant interaction between the ICRF heating wave and the ion, the energy exchange results in changes in P_ϕ and Λ according to [39, 40, 102]

$$\Delta P_\phi = \frac{N}{\omega} \Delta E, \tag{A.4}$$

$$\Delta \Lambda = (\Lambda_\infty - \Lambda) \frac{\Delta E}{E}, \tag{A.5}$$

where N is the toroidal mode number of the wave. If the cyclotron cold resonance line of the ICRF wave is located on axis, the parameter $\Lambda_\infty = 1$, whereas $\Lambda_\infty \neq 1$ if the cyclotron resonance line is located off axis. The parameter is given by $\Lambda_\infty = n\omega_{c0}/\omega$, where ω_{c0} is the cyclotron frequency on axis. For interactions between fast ions and waves of lower frequency, such as neoclassical tearing modes and Alfvén eigenmodes, equation (A.5) is replaced by $\Delta\mu = 0$. Such interactions have been studied extensively [13, 103–109], but are not considered in this work. From the relation between Λ and the ion pitch $p = v_\parallel / v$,

$$\Lambda = \left(1 - p^2\right) B_0 / B\left(R,z\right), \tag{A.6}$$

the streamlines in velocity space can be derived [23, 37], yielding

$$v_\perp^2 = \frac{1 - p_\infty^2}{p_\infty^2} v_\parallel^2 - \frac{p_0^2 - p_\infty^2}{p_\infty^2} v_0^2, \tag{A.7}$$

where

$$p_0^2 = 1 - \frac{B\left(R,z\right)}{B_0} \Lambda_0, \tag{A.8}$$

$$p_\infty^2 = 1 - \frac{B\left(R,z\right)}{B_0} \Lambda_\infty, \tag{A.9}$$

where the 0 subscript on p, v and Λ refers to their initial values, and the ∞ index refers to the asymptotic values for large energy gains. From (A.7), we can deduce the change in $v_\perp$ given a change in $v_\parallel$,

$$\Delta v_\perp = \frac{1 - p_\infty^2}{p_\infty^2} \frac{v_\parallel}{v_\perp} \Delta v_\parallel. \tag{A.10}$$

Appendix B. Regularisation parameter scans

Reconstructions of the fast-ion distribution function in discharge #86459 using first-order Tikhonov regularisation are shown in figure B1 for different regularisation parameters. All distributions are normalised independently to have a maximum at 1, as the diagnostics do not allow an absolute calibration [22]. All reconstructions show the same tendencies such as a tilt of the tail, a bump-on-tail and the decay of the tail around the barrier region, as presented in section 4.

Reconstructions of the fast-ion distribution function in discharge #86459 using both ICRF regularisation and collision-physics regularisation are shown in figure B2 for different

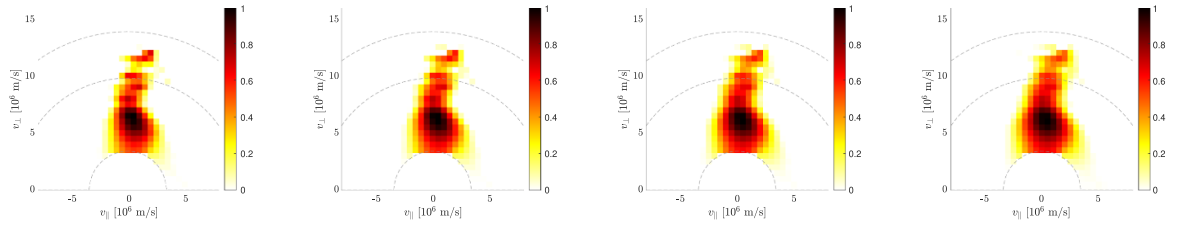

(a) $\lambda = 5 \cdot 10^3$ (b) $\lambda = 7 \cdot 10^3$ (c) $\lambda = 8 \cdot 10^3$ (d) $\lambda = 10 \cdot 10^3$

Figure B1. Reconstructions of the fast-ion distribution function in normalised units in discharge #86459 using first-order Tikhonov regularisation. Each subcaption denotes the regularisation parameter λ for each reconstruction. All distributions are normalised independently to have a maximum at 1.

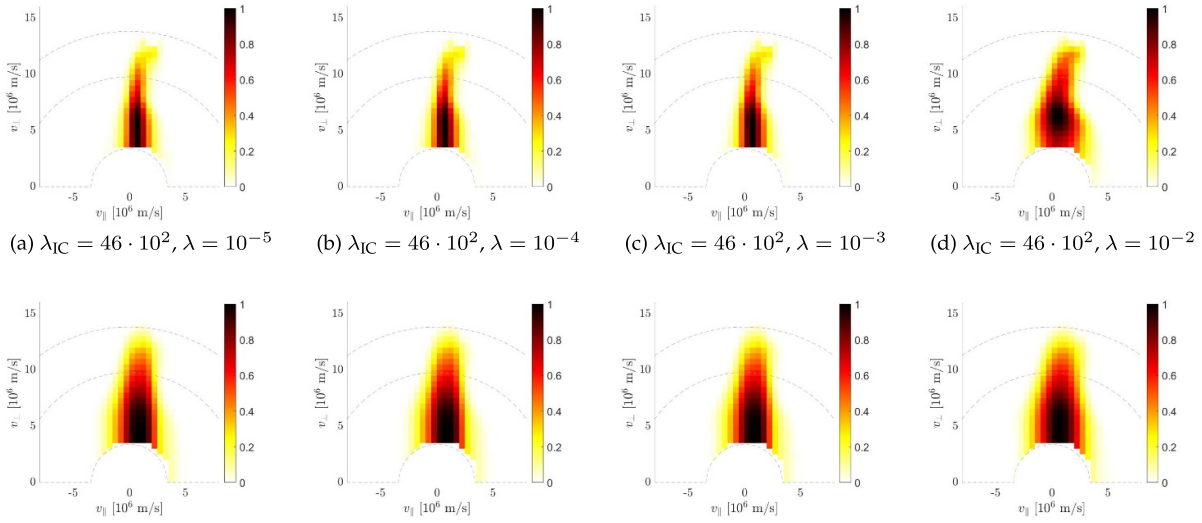

(a) $\lambda_{\mathrm{IC}} = 46 \cdot 10^2, \lambda = 10^{-5}$ (b) $\lambda_{\mathrm{IC}} = 46 \cdot 10^2, \lambda = 10^{-4}$ (c) $\lambda_{\mathrm{IC}} = 46 \cdot 10^2, \lambda = 10^{-3}$ (d) $\lambda_{\mathrm{IC}} = 46 \cdot 10^2, \lambda = 10^{-2}$

(e) $\lambda_{\mathrm{IC}} = 215 \cdot 10^2, \lambda = 10^{-5}$ (f) $\lambda_{\mathrm{IC}} = 215 \cdot 10^2, \lambda = 10^{-4}$ (g) $\lambda_{\mathrm{IC}} = 215 \cdot 10^2, \lambda = 10^{-3}$ (h) $\lambda_{\mathrm{IC}} = 215 \cdot 10^2, \lambda = 10^{-2}$

Figure B2. Reconstructions of the fast-ion distribution function in normalised units in discharge #86459 using both ICRF regularisation and collision-physics regularisation. Each subcaption denotes the regularisation parameters λ_{IC} and λ in a compact notation for each reconstruction. All distributions are normalised independently to have a maximum at 1.

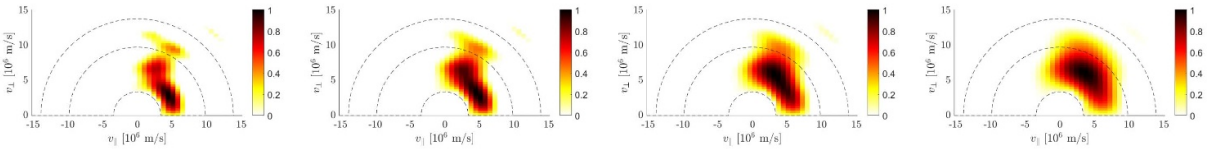

(a) $\log_{10}(\lambda) = -2.0$ (b) $\log_{10}(\lambda) = -1.7$ (c) $\log_{10}(\lambda) = -1.3$ (d) $\log_{10}(\lambda) = -1.0$

Figure B3. Reconstructions of the fast-ion distribution function in normalised units in discharge #95679 using first-order Tikhonov regularisation. Each subcaption denotes the regularisation parameter λ for each reconstruction. All distributions are normalised independently to have a maximum at 1.

regularisation parameters. Increasing the ICRF regularisation strength can diminish the small tilt of the tip of the tail as is evident when comparing the top and bottom row of figure B2, and the tail appears more smooth than in figure B1. Otherwise, the reconstructions appear consistent across the regularisation parameter scan.

Reconstructions of the fast-ion distribution function in discharge #95679 using first-order Tikhonov regularisation are shown in figure B3 for different regularisation parameters. The reconstructions show a definite tendency towards positive pitches, as expected from the three-ion scheme. However, the expected tail appears as disjoint blobs in subfigure (*a*), and with a bump-on-tail in subfigure (*b*). As the regularisation strength is increased towards subfigures (*c*) and (*d*) the entire distribution function is smoothened to such an extent that the narrow tail vanishes.

Reconstructions of the fast-ion distribution function in discharge #95679 using both collision-physics regularisation and ICRF-physics regularisation are shown in figure B4 for different regularisation parameters. Increasing the strength of the ICRF regularisation from the top to the bottom row smoothens out the tail towards positive pitches, whereas increasing the

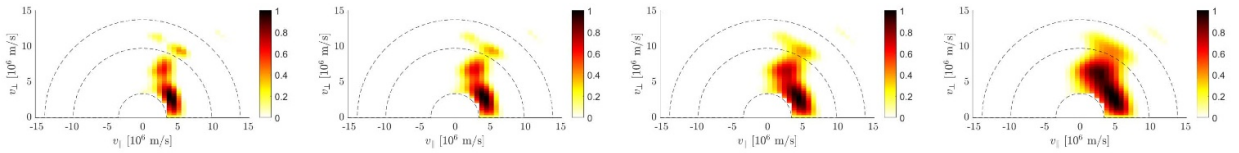

(a) $\log_{10}(\lambda_{\mathrm{IC}}, \lambda) = (-3.0, -3.0)$ (b) $\log_{10}(\lambda_{\mathrm{IC}}, \lambda) = (-3.0, -2.7)$ (c) $\log_{10}(\lambda_{\mathrm{IC}}, \lambda) = (-3.0, -2.3)$ (d) $\log_{10}(\lambda_{\mathrm{IC}}, \lambda) = (-3.0, -2.0)$

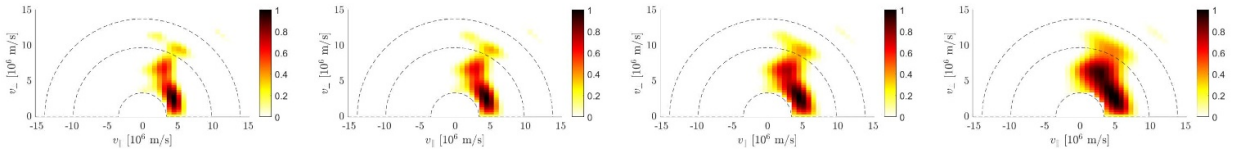

(e) $\log_{10}(\lambda_{\mathrm{IC}}, \lambda) = (-2.7, -3.0)$ (f) $\log_{10}(\lambda_{\mathrm{IC}}, \lambda) = (-2.7, -2.7)$ (g) $\log_{10}(\lambda_{\mathrm{IC}}, \lambda) = (-2.7, -2.3)$ (h) $\log_{10}(\lambda_{\mathrm{IC}}, \lambda) = (-2.7, -2.0)$

Figure B4. Reconstructions of the fast-ion distribution function in normalised units in discharge #95679 using both ICRF regularisation and collision physics regularisation. Each subcaption denotes the regularisation parameters λ_{IC} and λ in a compact notation for each reconstruction. All distributions are normalised independently to have a maximum at 1.

strength of the collision-physics regularisation, from the leftmost column to the rightmost column, smoothens out the distribution widening the tail. The tilt of the tail towards positive pitches is consistent through the entire regularisation parameter scan.

ORCID iDs

M. Rud 0000-0003-2482-4461
Y. Dong 0000-0001-8363-9448
L.-G. Eriksson 0009-0004-1375-9929
J. Eriksson 0000-0002-0892-3358
P.C. Hansen 0000-0002-7333-7216
H. Järleblad 0000-0003-1126-686X
Ye.O. Kazakov 0000-0001-6316-5441
D. Moseev 0000-0001-7955-8565
M. Nocente 0000-0003-0170-5275
B.C.G. Reman 0000-0003-3507-9444
A. Valentini 0009-0003-5394-4267
M. Salewski 0000-0002-3699-679X

References

[1] Heidbrink W.W. 2008 *Phys. Plasmas* **15** 055501
[2] Heidbrink W.W. and White R.B. 2020 *Phys. Plasmas* **27** 030901
[3] Gorelenkov N., Pinches S. and Toi K. 2014 *Nucl. Fusion* **54** 125001
[4] McClements K.G. and Fredrickson E.D. 2017 *Plasma Phys. Control. Fusion* **59** 053001
[5] Pinches S.D. *et al* 2015 *Phys. Plasmas* **22** 021807
[6] Todo Y. 2019 *Rev. Mod. Plasma Phys.* **3** 1
[7] Salewski M. *et al* 2025 *Nucl. Fusion* **65** 043002
[8] Hastie R.J. 1997 *Astrophys. Space Sci.* **256** 177–204
[9] Garcia-Munoz M. *et al* 2011 *Nucl. Fusion* **51** 103013
[10] Nabais F. *et al* 2010 *Nucl. Fusion* **50** 115006
[11] Heidbrink W.W. *et al* 2014 *Plasma Phys. Control. Fusion* **56** 095030
[12] Fredrickson E.D. *et al* 2009 *Phys. Plasmas* **16** 122505
[13] Podestà M. *et al* 2009 *Phys. Plasmas* **16** 056104
[14] Salewski M. *et al* 2012 *Nucl. Fusion* **52** 103008
[15] Salewski M. *et al* 2013 *Nucl. Fusion* **53** 063019
[16] Salewski M. *et al* 2014 *Nucl. Fusion* **54** 023005
[17] Weiland M. *et al* 2016 *Plasma Phys. Control. Fusion* **58** 025012
[18] Weiland M. *et al* 2017 *Nucl. Fusion* **57** 116058
[19] Salewski M. *et al* 2016 *Nucl. Fusion* **56** 106024
[20] Jacobsen A.S. *et al* 2016 *Plasma Phys. Control. Fusion* **58** 042002
[21] Jacobsen A.S. *et al* 2016 *Plasma Phys. Control. Fusion* **58** 045016
[22] Salewski M. *et al* 2017 *Nucl. Fusion* **57** 056001
[23] Reman B. *et al* 2025 *Nucl. Fusion* **65** 076007
[24] Järleblad H. *et al* 2025 *Nucl. Fusion* **65** 016060
[25] Madsen B., Salewski M., Huang J., Jacobsen A.S., Jones O. and McClements K.G. 2018 *Rev. Sci. Instrum.* **89** 10D125
[26] Harrison J. *et al* 2019 *Nucl. Fusion* **59** 112011
[27] Madsen B. *et al* 2020 *Nucl. Fusion* **60** 066024
[28] Madsen B. *et al* 2020 *Plasma Phys. Control. Fusion* **62** 115019
[29] Su J. *et al* 2021 *Plasma Sci. Technol.* **23** 095103
[30] Sun Y. *et al* 2024 *Nucl. Fusion* **65** 016040
[31] Geiger B. *et al* 2017 *Plasma Phys. Control. Fusion* **59** 115002
[32] Han J., Kim J., Kim M., Lee M., Kang J., Yoo J. and Sung C. 2024 *Fusion Eng. Des.* **207** 114639
[33] Salewski M. *et al* 2018 *Nucl. Fusion* **58** 096019
[34] Schneider M. *et al* 2016 *Nucl. Fusion* **56** 112022
[35] Kazakov Y., Van Eester D., Dumont R. and Ongena J. 2015 *Nucl. Fusion* **55** 032001
[36] Kazakov Y. *et al* 2020 *Nucl. Fusion* **60** 112013
[37] Kazakov Y.O. *et al* 2021 *Phys. Plasmas* **28** 020501
[38] Nocente M. *et al* 2020 *Nucl. Fusion* **60** 124006
[39] Eriksson L. and Helander P. 1994 *Phys. Plasmas* **1** 308–14

[40] Eriksson L.-G., Mantsinen M.J., Hellsten T. and Carlsson J. 1999 *Phys. Plasmas* **6** 513–8
[41] Fitzgerald M. and Breizman B. 2025 *Fundam. Plasma Phys.* **13** 100084
[42] Rud M. *et al* 2025 *Nucl. Fusion* **65** 056008
[43] Heidbrink W.W., Burrell K.H., Luo Y., Pablant N.A. and Ruskov E. 2004 *Plasma Phys. Control. Fusion* **46** 1855
[44] Eriksson J. *et al* 2018 *Plasma Phys. Control. Fusion* **61** 014027
[45] Maslov M. *et al* 2023 *Nucl. Fusion* **63** 112002
[46] Nocente M. *et al* 2022 *Rev. Sci. Instrum.* **93** 093520
[47] Kiptily V.G. *et al* 2022 *Plasma Phys. Control. Fusion* **64** 064001
[48] Mantsinen M.J. *et al* 2002 *Phys. Rev. Lett.* **88** 105002
[49] Kiptily V. *et al* 2010 *Nucl. Fusion* **50** 084001
[50] Nocente M. *et al* 2012 *Nucl. Fusion* **52** 063009
[51] Eriksson J. *et al* 2015 *Nucl. Fusion* **55** 123026
[52] Cottrell G.A. 2000 *Phys. Rev. Lett.* **84** 2397–400
[53] Mantsinen M. *et al* 2023 *Nucl. Fusion* **63** 112015
[54] Nocente M. *et al* 2019 *Plasma Phys. Control. Fusion* **62** 014015
[55] Heidbrink W.W., Luo Y., Burrell K.H., Harvey R.W., Pinsker R.I. and Ruskov E. 2007 *Plasma Phys. Control. Fusion* **49** 1457
[56] Stagner L. and Heidbrink W.W. 2017 *Phys. Plasmas* **24** 092505
[57] Järleblad H. *et al* 2021 *Rev. Sci. Instrum.* **92** 043526
[58] Järleblad H. *et al* 2022 *Nucl. Fusion* **62** 112005
[59] Järleblad H. *et al* 2024 *Comput. Phys. Commun.* **294** 108930
[60] Järleblad H. *et al* 2024 *Nucl. Fusion* **64** 026015
[61] Moseev D., Salewski M., Garcia-Muñoz M., Geiger B. and Nocente M. 2018 *Rev. Modern Plasma Phys.* **2** 7
[62] Heidbrink W.W. 2010 *Rev. Sci. Instrum.* **81** 10D727
[63] Salewski M. *et al* 2014 *Plasma Phys. Control. Fusion* **56** 105005
[64] Salewski M. *et al* 2011 *Nucl. Fusion* **51** 083014
[65] Salewski M. *et al* 2018 *Fusion Sci. Technol.* **74** 23–36
[66] Salewski M. *et al* 2019 *J. Instrum.* **14** C05019
[67] Salewski M. *et al* 2015 *Nucl. Fusion* **55** 093029
[68] Salewski M. *et al* 2016 *Nucl. Fusion* **56** 046009
[69] Jacobsen A. *et al* 2015 *Nucl. Fusion* **55** 053013
[70] Jacobsen A.S. *et al* 2017 *Rev. Sci. Instrum.* **88** 073506
[71] Galdon-Quiroga J. *et al* 2018 *Plasma Phys. Control. Fusion* **60** 105005
[72] Schmidt B.S. *et al* 2024 *Plasma Phys. Control. Fusion* **66** 045004
[73] Schmidt B.S. *et al* 2021 *Rev. Sci. Instrum.* **92** 053528
[74] Schmidt B.S. *et al* 2023 *Phys. Plasmas* **30** 092109
[75] Heidbrink W.W., Garcia A., Boeglin W. and Salewski M. 2021 *Plasma Phys. Control. Fusion* **63** 055008
[76] Valentini A. *et al* 2025 *Nucl. Fusion* **65** 112001
[77] Rud M. *et al* 2024 *Nucl. Fusion* **64** 036007
[78] Eriksson J., Conroy S., Andersson Sundén E. and Hellesen C. 2016 *Comput. Phys. Commun.* **199** 40–46
[79] Tardocchi M. *et al* 2011 *Phys. Rev. Lett.* **107** 205002
[80] Gatu J.M. *et al* 2006 *Rev. Sci. Instrum.* **77** 10E702
[81] Gatu J.M. *et al* 2008 *Nucl. Instrum. Methods Phys. Res.* A **591** 417–30
[82] Binda F., Ericsson G., Eriksson J., Hellesen C., Conroy S. and Sundén E.A. 2014 *Rev. Sci. Instrum.* **85** 11E123
[83] Valentini A. *et al* 2024 *Nucl. Fusion* **65** 026001
[84] Valentini A. *et al* 2024 *Rev. Sci. Instrum.* **95** 083551
[85] Valentini A. *et al* 2025 *Nucl. Fusion* **65** 046031
[86] Hirvijoki E., Asunta O., Koskela T., Kurki-Suonio T., Miettunen J., Sipilä S., Snicker A. and Äkäslompolo S. 2014 *Comput. Phys. Commun.* **185** 1310–21
[87] Giacomelli L., Belli F., Binda F., Conroy S.W., Eriksson J., Milocco A., Popovicev S. and Syme D.B. 2018 *Rev. Sci. Instrum.* **89** 10I113
[88] Breslau J. *et al* 2018 TRANSP [Computer Software] (available at: https://doi.org/10.11578/dc.20180627.4)
[89] Dendy R.O., Hastie R.J., McClements K.G. and Martin T.J. 1995 *Phys. Plasmas* **2** 1623–36
[90] Bilato R., Odstrcil T., Casson F.J., Angioni C., Brambilla M., Kazakov Y.O. and Poli E. 2017 *Nucl. Fusion* **57** 056020
[91] Hadamard J. 1902 *Princeton Univ. Bull.* **13** 49–52
[92] Tikhonov A.N. 1963 *Sov. Dok.* **4** 1035–8
[93] Hansen P.C. 2010 *Discrete Inverse Problems: Insights and Algorithms* (Society for Industrial and Applied Mathematics)
[94] Schmidt B. *et al* 2023 *Nucl. Fusion* **63** 076016
[95] Gaffey J.D. 1976 *J. Plasma Phys.* **16** 149–69
[96] Core W. 1993 *Nucl. Fusion* **33** 829
[97] Rud M. *et al* 2024 *Nucl. Fusion* **64** 076018
[98] Moseev D. and Salewski M. 2019 *Phys. Plasmas* **26** 020901
[99] Hellesen C., Mantsinen M., Conroy S., Ericsson G., Eriksson J., Kiptily V.G. and Nabais F. 2018 *Nucl. Fusion* **58** 056021
[100] Stagner L. *et al* 2022 *Nucl. Fusion* **62** 026033
[101] Hyvärinen O. *et al* 2025 *Nucl. Fusion* **65** 092003
[102] Hellsten T., Johnson T., Carlsson J., Eriksson L.-G., Hedin J., Laxåback M. and Mantsinen M. 2004 *Nucl. Fusion* **44** 892
[103] Gorelenkov N.N., Cheng C.Z. and Fu G.Y. 1999 *Phys. Plasmas* **6** 2802–7
[104] Podestà M., Gorelenkova M. and White R.B. 2014 *Plasma Phys. Control. Fusion* **56** 055003
[105] Podestà M., Gorelenkova M., Gorelenkov N.N. and White R.B. 2017 *Plasma Phys. Control. Fusion* **59** 095008
[106] Podestà M. *et al* 2022 *Nucl. Fusion* **62** 126047
[107] Podestà M. *et al* 2021 *Plasma Phys. Control. Fusion* **64** 025002
[108] Todo Y., Van Zeeland M.A., Bierwage A., Heidbrink W. and Austin M. 2015 *Nucl. Fusion* **55** 073020
[109] Chen L. and Zonca F. 2016 *Rev. Mod. Phys.* **88** 015008